Tong, L., Yuan, J., Zhang, Z. *et al.* Nanoscale subparticle imaging of vibrational dynamics using dark-field ultrafast transmission electron microscopy. *Nat. Nanotechnol.* (2022). https://doi.org/10.1038/s41565-022-01255-5

# Nanoscale Subparticle Imaging of Vibrational Dynamics Using Dark Field Ultrafast Transmission Electron Microscopy

Ling Tong[1,2,], Jun Yuan[3], Zhiwei Zhang[1,2], Jau Tang[4], Zhiwei Wang[1,2,5*]

[1]Beijing Institute of Nanoenergy and Nanosystems, Chinese Academy of Sciences, Beijing 100083, P. R. China

[2]School of Nanoscience and Technology, University of Chinese Academy of Sciences, Beijing 100049, P. R. China

[3]School of Physics, Engineering and Technology, University of York, York, UK

[4]The Institute for Technological Sciences, Wuhan University, Wuhan 430072, China.

[5]Center on Nanoenergy Research, School of Physical Science and Technology, Guangxi University, Nanning 530004, P. R. China

**Corresponding Author**

* e-mail: wangzhiwei@ucas.ac.cn

**Abstract.**

Understanding of nanoscale energy transport and acoustic response is important for applications of nanomaterials, but hinges on complete characterization of their structural dynamics. However, a precise determination of structural dynamics within nanoparticles is still challenging, requiring high spatiotemporal resolution and detection sensitivity. Here, we present an ultrafast transmission electron microscope based centered dark-field imaging approach that is capable of directly mapping the picosecond scale evolution of intra-nanoparticle vibration with spatial resolution down to 3 nm. Using this approach, we investigated the photo-induced vibrational dynamics in individual Au heterodimers, composed of a nanoprism and a nanosphere. We not only observed the retardation of in-plane vibrations in the nanoprisms, which we attribute to thermal and vibrational energy transferred from adjacent nanospheres mediated by coatings, but also the existence of complex multimodal oscillation and its spatial variation within individual nanoprisms. This work represents an advance in real-space mapping of the vibrational dynamics on the subnanoparticle level with high detection sensitivity.

.

Ultrafast transmission electron microscopy (UTEM or 4D-TEM) is an emerging technology capable of imaging structural dynamics in real-space, which combines the high spatial resolution of electron imaging and the high temporal resolution of femtosecond lasers[1-2]. UTEM has been used for direct observations of transient bend contours and strain wave evolutions in micrometer-scale specimens and acoustic vibrational modes in Au nanorods through bright-field (BF) or (off-axis) dark-field (DF) imaging modes[3-11]. Nevertheless, because of inherent Coulomb repulsion among the pulsed electrons within the same bunch, there exists an upper limit for the number of electrons per pulse (usually tens of electrons) available for UTEM imaging before spatial and temporal coherence deteriorate[1,3]. Imaging with a low electron number per pulse poses challenges in the image analysis, especially for those dynamic processes with a weak optical response or multiple modal structures. Dynamical diffraction effect and inelastic electron scattering processes also complicate the interpretation of the resulting contrast variation[12], resulting in a considerable barrier on the identification of spatial oscillation evolution inside nanoparticles. As a result, most structural dynamics studies to date are by transient optical spectroscopy or ultrafast electron diffraction performed at nanoparticle or nanoparticle assembly levels[13-15]. Nevertheless, they have already revealed complex structural responses especially for particles with sizes less than 100 nm[13-20]. As vibrational dynamics are easily influenced by surface configuration, polymorphism, interparticle coupling, capping agents, and substrate interactions, high resolution study of variation of structural dynamics within the nanoparticles would be of great interest, but they have been successful only at some

special sites featuring vibrational hotspots[9-10].

Here we describe an ultrafast high-sensitivity centered dark-field (UHS-CDF) imaging approach, which, by optimizing the probing and imaging optics, enables an efficient collection of pulsed electrons and, simultaneously, a considerable reduction of the undesired contribution from the substrate and beam absorption. Using this UHS-CDF imaging approach, we investigated acoustic vibration dynamics in Au heterodimers composed of triangularly shaped nanoprisms and nanospheres. We observed vibrational coupling at the nanosphere/nanoprism interface, as evidenced by the formation of two fully separated peaks in Fourier spectra. We determine that the vibrational coupling arises between the fundamental breathing mode of the nanoprism and the quadrupolar mode of the nanosphere. More importantly, we also show that the spatial variation of nanoprism oscillations can be resolved at the scale down to ~3 nm, demonstrating the feasibility of a reliable study of intra-particle dynamics analysis by UHS-CDF imaging.

**UHS-CDF imaging technique**

The experimental setup for ultrafast TEM imaging is schematically illustrated in Figure 1a. Optical pulses from a femtosecond laser (with a 210 fs pulse width and a 1035 nm center wavelength) are split into two beams, followed by their introduction into UEM chambers to excite the specimen (frequency doubled) and generate pulsed electrons (frequency quadrupled)[21]. The electron waves passing through the sample were recorded by the UHS-CDF imaging approach (see Supplementary methods for details). In brief, UTEM imaging was carried out by adopting a slightly converged (instead of

parallel) pulsed electron beam and a corresponding (large-size) objective aperture with the samples tilted approximately to a two-beam condition. Only the diffracted beam travels along the optic axis and passes through the objective aperture. This is to be distinguished from the off-axis DF, for example used in the study of structural phase transitions in the 1T-polytype of $TaS_2$.[11] The imaging intensity of Au nanoprisms recorded in this way increases by at least one order of magnitude in comparison with the standard DF mode (Supplementary Fig. 3). Our approach has been compared with the complementary BF-UTEM technique by both experimental observation and time-resolved multislice image simulation (Supplementary Methods, Supplementary Figs. 5-12, and Supplementary Videos 1-4). UHS-CDF imaging exhibits better signal-to-noise ratios because it is less affected by absorption and the considerable suppression of the dynamics contributions from the substrate which diffracts in different angles. Hence, the oscillation information intrinsic to the nanocrystals can be extracted from a more localized region in comparison with the corresponding BF imaging. As we demonstrate below UHS-CDF is ideally suited for refined structural dynamics analysis of inter and intra nanoparticle dynamics where either the photo-induced dynamical changes are either intrinsically small or muted because of multimodal oscillations. The possible exceptions for all these diffraction contrast methods are those nanostructures not firmly anchored to the supporting substrates (e.g., nanospheres), as the imaging contrast is now not only sensitive to photoinduced vibrations, but also the unavoidable drift of crystallographic orientations under continuous electron beam and/or laser irradiations.

**Substrate effect on vibrational dynamics**

Through UHS-CDF imaging, we first determined the structural dynamics characteristics of individual Au nanoprisms on three different substrates (graphite flakes, 2D-graphene, and $Si_3N_4$ membranes) under identical pumping conditions (2.8 mj/cm$^2$). Fig. 1b shows strong temporal variations in the relative image intensity ratio $I/I_0$ (pumped to non-pumped intensity ratio) integrated over the image areas for isolated Au nanoprisms supported on graphite and graphene substrate respectively. Strong acoustic vibrations were observed immediately after optical impingement, with the relative amplitude of image contrast variation in excess of 50%. The power spectral density analysis shows a well-defined mode frequency of 17.6 GHz for photo-induced oscillation in Au nanoprisms on graphite. This frequency is close to that of the fundamental in-plane dilation mode along triangular bisectors of Au nanoprisms[22], with expected size dependence (Supplementary Fig. 13). This is to be contrasted with equally strong photo-induced multiple-mode oscillation with comparatively lower frequencies for the dynamics of Au on graphene. In contrast, Au nanoprisms on the Si3N4 substrate do not exhibit obvious in-plane oscillations, with its power spectral density mostly consisting of those random image intensity fluctuation possibly induced by system instabilities (Fig. 1c and Supplementary Fig. 14). By means of monochromatic electron energy-loss spectroscopy (EELS) and finite element analyses, we find that the variety of vibrational responses is related to optical pump conditions, heat dissipation characteristics of Au nanoprisms, and substrate interactions (see

Supplementary Notes for details). To exclude the dynamic complexity introduced by absorptive and conductive (graphite and graphene) substrates, we prepared Au nanoprism-nanosphere heterodimers with $Si_3N_4$ adopted as substrates for the vibrational interaction study.

**Retarded vibrations in Au nanoprisms**

Fig. 2 shows typical structural dynamics observations of Au heterodimers on $Si_3N_4$ substrates. The average length of the three long sides of the truncated nanoprism and the diameter of the nanosphere are 40 and 44 nm, respectively. The nanoparticles are protected by a layer of CTAC (hexadecyltrimethylammonium chloride) surfactants, as marked with the arrows in the bright-field TEM image in Fig. 2a (and Supplementary Fig. 16). The direct visualization of these capping agents by the UTEM even without a field-emission gun is partly attributed to the addition of a heavier, shape-directing agent (potassium iodides)[23-24]. The inter-nanoparticle spacing is measured to be 1.3 nm, which corresponds to the chain length of a single CTAC molecule[25]. Fig. 2b shows a UHS-CDF image recorded at time zero using a g(220) diffraction as indicated in Fig. 2c. The $I/I_0$-t trace in Fig. 2d (see also Supplementary Video 5) was extracted from the rectangular region marked in Fig. 2b, which displays an immediate Debye−Waller intensity attenuation subsequent to optical excitation. The following energy relaxation does not lead to a marked periodic oscillation until at about 355 ps, when a regular vibration occurs abruptly. By a careful recalibration before and after UHS-CDF experiments (Supplementary Fig. 17), we excluded the possibility of a drift in the time

zero. For the periodically oscillatory time series, the change in relative intensity (~10%) is much smaller than that of individual nanoprisms on graphene/graphite flakes, and the power spectral density analysis (Fig. 2d, inset) displays three distinct frequency peaks at 25.3 and 9.3, and 1.6 GHz.

For metal nanostructures, acoustic vibrations are generally launched by hot electron pressure and lattice anharmonicity emerging during the course of electron and lattice thermalization[26-27]. This usually leads to the initiation of vibrations within about 10 ps[13, 27-28]. However, we observed significant retardation of the oscillation initiation spanning from approximately 150 to 600 ps regardless of the size or configuration of nanoparticle aggregates examined in our UHS-CDF imaging experiments (Supplementary Fig. 18). A previous investigation of graphene-supported Au nanorods also demonstrated the delayed initiation of acoustic oscillations (~400 ps). This was attributed to the photoinduced commensurate-to-incommensurate transition of Au-graphene crystalline interfaces[10]. This mechanism does not apply to our observations because the $Si_3N_4$ substrate supporting Au heterodimers features an amorphous structural configuration. The Debye-Waller factor may change with time, due to temperature variation, but its impact would be gradual, so it can not explain the sudden onset of the retarded oscillation.

To figure out the cause of the initiation retardation observed in the Au nanoprisms on $Si_3N_4$ substrates, we combined with numerical simulations to analyze the temperature

evolution of the whole heterodimers during the relaxation after photo-excitation. Based on a two-temperature modelling approximation and with reference to the actual geometries of the heterodimer in Fig. 2a, the temporal change in both electron ($T_e$) and lattice ($T_l$) temperatures was calculated and plotted in Fig. 3a (and Supplementary Fig. 20). The comparatively more marked temperature elevation in the nanosphere is associated with its stronger LSPR excitation and consequently larger optical absorption cross sections (Supplementary Fig. 19). The highest lattice temperatures (nanosphere: 573 K; nanoprism: 496 K) are reached at ~20 ps through electron and phonon interactions. With the lattice temperature maxima set as initial values, the heat transfer behaviors of the entire heterodimer-substrate system can be simulated. As shown in Fig. 3b, a more precipitous temperature drop is clearly present in the nanoprism due to its much larger contact area with $Si_3N_4$ substrates that facilitates rapid heat transport. For the surfactants at the nanosphere-nanoprism interface, a gradual temperature decrease occurs from the nanosphere side (initially in molten state) to the other. In contrast to the nanoprism, the nanosphere (and its adjacent surfactants) exhibits a slow temperature variation. The surfactants approach their solidification point (~507 K) between 300 and 400 ps, as shown in Fig. 3c.

Further understanding can be achieved by correlating the numerical calculation results to the UHS-CDF experimental observations of Au heterodimers. Once the solidification point of the capping agents is reached, an abrupt increase in the elastic modulus, speed of sound, thermal conductivity, etc. is expected to occur[29-32]. Solidification of the

surfactants thus enables a much more efficient propagation of vibrational energy from the nanosphere to the nanoprism. The accelerated heat transfer between the two nanoparticles with a large temperature discrepancy should also occur at the same time, further promoting lateral lattice anharmonicity in the nanoprism. Hence, the sharp changes in both vibrational and thermal properties should be the major cause for the retarded launching of in-plane oscillations. The energy transfer could also be mediated by the underlying substrates[33], but this process would proceed continuously in any case with a limited effect. A schematic representation of the transient structural dynamics process arising in the heterodimer is shown in Fig. 3d, and a more detailed analysis of vibrational modes is provided in Supplementary Notes.

**Intra-nanoparticle analysis of vibrational dynamics and interactions**

UHS-CDF imaging enables us to have a closer examination of the dynamics inside the nanoprism, by which a marked spatial variation of the vibration amplitudes is revealed. This is evident from the intensity standard deviation (ISD) maps generated based on the portion of the time series featuring regular vibrations (Fig. 4a). Overall, the oscillations decay from the left surface (S1) to the nanoprism-nanosphere interface (Fig. 4b), and the largest intensity modulation occurs at the region P1 marked in Fig. 4a. The ISD patterns do not conform to the characteristics expected of either unidirectional wave propagations or periodic specimen tilting (as no contrast change would appear in the ISD maps under both circumstances). On the other hand, this phenomenon is consistent with the formation of a standing phonon-wave with its antinode at S1. Line

L1, which passes through P1 and interfacial contact sites and is approximately parallel to the bottom surface, represents the principal propagation direction of any elastic wave emitting from the interface between the nanoprism and the nanosphere. By approximating the nanoprism along L1 as a mass loaded rod, the equivalent mass factors involving the contribution from the nanosphere, surfactant, and substrate can be determined (Supplementary Notes and Supplementary Fig. 22).

A further analysis, however, illustrates that the vibrations do not fully conform to the nature of standard standing waves in solids. Fig. 4c shows temporal $I/I_0$ traces measured from the regions P1 (pink curve) and P10 (green curve, near to ISD minimum) indicated in Fig. 4a. The variation of oscillation frequency is clearly present in their power spectral density analyses (Fig. 4c, insets). We find that this phenomenon occurs partially due to the formation of vibrational coupling between the two components of the heterodimer. Fig. 4d shows a spatially resolved oscillation analysis along line L1 for the primary vibrational frequency displayed in P1 (25.2 GHz). Three characteristic zones (1-3) can be clearly identified (Fig. 4d and 4e). In Zone-1, which spans approximately 22 nm from the left end, all the regions (P1-P6) exhibit a single frequency peaked at 25.2 GHz. Most of them have a considerably narrower linewidth than that displayed in the overall measurements (Fig. 2d, inset) that represents a superposition effect of all three zones. In contrast, Zone-3 (spanning ~17 nm from the right end) displays two fully separated peaks $f_{c+}$ and $f_{c-}$, located at 27.0 and 21.9 GHz, respectively. The frequencies remain basically constant throughout this zone,

suggesting that a rather uniform internanoparticle interaction field be established. We further analyzed the behaviors of the coupling dynamics by employing a coupled harmonic oscillator model. This leads to the determination of the oscillation frequency of the nanosphere participating in the vibrational interaction and the coupling rate, which are 20.8 and 2.9 GHz, respectively (Supplementary Notes). The derived frequency for the nanosphere is close to the experimental frequency (20.5 GHz) measured from a section of the nanosphere (Supplementary Notes, and Supplementary Fig. 23). A comparison with finite-element eigenfrequency analysis (Supplementary Fig. 24) suggests that the l=2 shear mode of the nanosphere mainly contribute to the internanoparticle coupling.

Between these two zones, we can recognize the presence of an intermediate transition region (Zone-2), in which two frequency peaks ($f_+$ and $f_-$) are still observed, but they exhibit less separation (see also Supplementary Video 6). With the increasing distance from Zone-1, both peaks exhibit a gradual red shift (more obvious for $f_-$), ultimately resulting in the coupled peaks $f_{c+}$ and $f_{c-}$. In addition, the frequency gap $\Delta f$ (=$f_+$ - $f_-$) displays an increase near the interface (Fig. 4d, Zone-2 inset), which could be mainly caused by the enhanced coupling strengths at the position (Supplementary Fig. 25). The formation of a transition zone may be a consequence of transient energy optimization within the nanoprism after laser excitations. It functions as a spatial buffer region for minimizing the dramatic discrepancy of displacement fields between Zones 1 and 3. In addition, considering that only a part of the nanoprism is coupled elastically to the sphere, with a moderate coupling strength, synchronization between the two nanoparticles may also occur through the $Si_3N_4$ substrates. This effect could be superimposed onto the coupled harmonic oscillation, leading to the actually rather complicated spatial evolution of vibrations in the nanoprism, e.g., the appearance of a high-order overtone (41.1 GHz) in the power spectral density for P10. Hence, the

$Si_3N_4$ substrate, despite its light transparency and insulation, may still play a role in the observation of the multiple characteristic zones and abundant interaction dynamics.

In comparison with overall measurements of vibrational dynamics by ultrafast optical spectroscopy/microscopy (Supplementary Notes), it is clear that an analysis of the intra-nanoparticle dynamics provides more detailed information about the vibrational interactions. To examine how locally the vibration dynamics can be identified by UHS-CDF imaging without suffering from the severe effect of background noises, we conducted an oscillation analysis around the primary frequency peak by adopting varying sizes of concentric square regions at Zone-1. As shown in Fig. 4f, no obvious dynamic change occurs when the size of the selected region is reduced from 10 nm to 2 nm across. However, a prominent noise effect was observed at the smallest region (1 nm), in which a spurious peak become clearly visible at 28.7 GHz. Fig. 4g shows the oscillation measurements from three side-by-side square regions with side lengths of 3 nm near the boundary of Zones 1 and 2 (as marked in the insert). From S1 to S3, a clear tendency exists that the primary frequency peak becomes wider and then slightly separated. These measurements, therefore, demonstrate that the spatial oscillation evolution can be accurately resolved down to 1-3 nm using our experimental current settings, despite the rather weak and rich vibrational behaviors presented in the heterodimer interactions. Under the identical optical excitation conditions, we also recorded BF-UTEM images on the same nanoparticles, which displays a lower and complex dynamics contrast (Supplementary Fig. 26). By combining the UHS-CDF

imaging approach with the advances in instrumentation[10], further improvement in both the detection sensitivities and the spatial resolution could be envisaged. It may allow the vibrational interactions to be inspected more locally and on a smaller time scale.

**The effect of nanocrystal deformation**

We can also illustrate the strong effect of nanocrystal deformation on the transient dynamic responses of $Si_3N_4$-supported Au heterodimers. Fig. 5a shows a BF-TEM image of a Au heterodimer (nanoprism side length: 44 nm; nanosphere diameter: 37 nm), in which the nanoprism displays a bending deformation as reflected in the non-uniform diffraction contrast in the UHS-CDF image recorded at time zero (Fig. 5b). The considerably lower contrast presented on the right side is caused by its larger excitation error regarding the g(220) Bragg diffraction for imaging in the bent part. A temporal analysis of the oscillation intensity (Fig. 5d top panel) indicates that the retarded oscillation occurs more prominently at the right half side ($S_R$). The highest amplitude (antinode) is found near the top corner in the principal propagation direction, but most of the regions at the surface (S1) far from the interface, as indicated with the square bracket in Fig. 5c, P3, do not exhibit the notable vibrations as observed in Fig. 4a. This phenomenon could be related to the presence of structural imperfections, most likely localized lattice strain and a deflection of the vibrational standing wave from the bent section, which leads to the attenuation of the vibration amplitudes at the surface S1. The nanoprism deformation appears also to cause a considerable decrease of vibrational coupling strengths, as no prominent frequency separation can be detected at

the interface (Supplementary Fig. 27). Lastly, we also conducted UHS-CDF imaging with controllable pump polarizations. Fig. 5d (bottom) shows the I-t trace measured after the pump polarization has been changed from M1 to N1 (as marked in Fig. 5a). No obvious difference in the oscillation behaviors is detected between the two polarizations, suggesting insignificant contributions from the polarization-related plasmon resonances in the nanoprism and a weak coupling of the plasmons between nanoprisms and nanospheres. Similar result is obtained from the polarization analysis of the nondefective nanoparticles as displayed in Supplementary Fig. 28. These control experiments, hence, further support that the enhanced oscillation of nanoprisms occurs as a result of vibrational/thermal energy propagation from nanospheres.

**Conclusions**

We have shown that spatially resolved oscillation dynamics within individual nanoparticles can be determined with resolution down to 3 nm via UHS-CDF imaging. This is thanks to the high dynamics signal contrast achieved through optimization of dark field imaging conditions as well as a considerable suppression of the unrelated substrate contribution. By investigating the vibrational dynamics within the Au heterodimers composed of nanospheres and nanoprisms on silicon nitride substrate, we observed the frequency coupling of acoustic vibrations between the nanoprisms and nanospheres and the retarded initiation of enhanced vibration in nanoprism indicative of vibrational and thermal energy transfer from nanospheres after optical excitation. However, uncoupled acoustic vibration can be found to co-exist with the coupled

acoustic vibration within the same nanoprisim and the relation between them can be different if the nanoprism is deformed. The complex multimodal dynamic phenomena within nanoparticles open a new field of intraparticle acoustics phononics and their possible manipulation through engineering of surfaces, interfaces, structural defects or other boundary conditions in the future. The spatial and temporal complexities of the vibration dynamics uncovered in our study suggest the importance of going beyond the existing nanoparticle level characterization by spectroscopy and diffraction intensity analysis.

## Acknowledgments

This research was supported by the National Natural Science Foundation of China (Grant Nos. 11774032 and 51571035). We thank Deshuai Li, Xiaofang Kang and John Spencer Baskin for their help in UTEM experiments, and Drs. Peng Wang and Si Gao for EELS experiments.

## Author contributions

Z.W.W. conceived the idea. L.T., and Z.W.W. performed the UTEM experiments. L.T., Z.W.W. and J.T. conducted the UTEM data analysis. L.T, Z.W.Z., Z.W.W., and J. Y. carried out numerical simulation and analysis. All authors discussed the results. Z.W.W., L.T. and J. Y. wrote the manuscript with input and comments from all authors.

## Competing interests

The authors declare no competing interests.

**Figure Legends/Captions**

**Fig. 1. Schematic of the UHS-CDF imaging setups and structural dynamics of isolated Au nanoprisms on various substrates. a**, A schematic description of the ultrafast TEM imaging system. Two laser beams generated from the same femtosecond laser are introduced into the TEM column to excite the samples and create electron packets. Inside the column, the electron optics ray for UHS-CDF imaging is schematically illustrated. (SHG: second harmonic generation; FHG: fourth harmonic generation. CL: Condenser lenses; DEF: Deflection coils; OL-pre: Objective lens prefield; OL-post: Objective lens postfield; OA: Objective aperture; IL: Intermediate lens; PL: Projector lens). **b**, Temporal evolution in the relative image intensity of individual Au nanoprisms on graphite flake and graphene substrates respectively. The insets show the power spectral densities of the oscillatory signal for the former and the whole trace for the latter. **c**, Temporal $I/I_0$ trace for an Au nanoprism on $Si_3N_4$ substrate. The inserted image shows an individual frame recorded at time zero. The inserted figure is the power spectral density of the whole trace.

**Fig. 2. Overall structural dynamics of an Au nanoprism-nanosphere heterodimer on $Si_3N_4$ substrate**. **a**, A BF-TEM image recorded at the thermionic emission mode. The arrows indicate the CTAC surfactant coatings. **b**, A UHS-CDF image (t=0) recorded with a g(220) diffraction spot as indicated **c**, Temporal variation in the integrated relative image intensity extracted from the rectangular region marked in **b**. A damped harmonic oscillation fit (thicker solid line) is overlayed on the oscillatory section (355-920 ps) and the insert display the corresponding frequency power spectrum. PSD: power spectral density. The intensity standard deviation in the whole negative time range is 2.5% (as marked with the arrow).

**Fig. 3. Numerical simulation of thermal evolution in hetrodimers**. **a**, Two-temperature model calculation of the time-dependence of the electron and lattice temperatures, respectively, for an isolated Au nanoprism and an isolated nanosphere with sizes identical to those in Fig. 2a. **b**, Time-dependent temperature change in different components of the heterodimer, determined from a heat-transfer finite element

simulations (the indentation depth of Au nanosphere is 0.1 nm). **c**, Spatial temperature distribution displayed for the relaxation time at 355 ps. **d**, Schematic illustration of the structural dynamics associated with the phase change of surfactants following fs laser excitations.

**Fig. 4**. **Intra-nanoparticle oscillation analysis of the Au nanoprism in a heterodimer on $Si_3N_4$ substrate.** **a**, An intensity standard deviation (ISD) map generated from the oscillatory section of the nanoprism in Fig. 2d. **b**, a 3D surface plot of the ISD map in **a**. The coordinate axes placed at the bottom-left corners indicate their orientation relationship. **c**, $I/I_0$ traces extracted from regions P1 and P10 as marked in **a** (P10 is indicated by a red arrow). The damped harmonic oscillation fits (thicker solid lines) are overlayed on top of the oscillatory sections whose power spectral densities are shown in insets, respectively. The frequency 41.1 GHz in P10 corresponds to an overtone of the (coupled) primary vibrational mode. **d**, Vibrational dynamics measured along line L1 marked in **a** around the primary vibrational frequency (25.2 GHz). The inset to the middle panel displays the change in frequency separation ($f_+ - f_-$) of two coupled modes with the varying distance from the interface (P7-11). All the intensity data in **c** and **d** were obtained from a square region with a side length of 7.5 nm, except for P10 in **c** for which a side length of 15 nm is used. **e**, Schematic display of the three characteristic zones found in the nanoprism. **f-g**, Power spectral densities of oscillatory section averaged over five concentric square regions (with side lengths of 10, 5, 3, 2, and 1 nm) at Zone-1 or three 3 nm-size square regions (S1-S3) side by side near the interface of Zone-1 and Zone-2, as marked in the insets.

**Fig. 5**. **Effect of structural deformation on vibrational interactions of Au nanoparticles on $Si_3N_4$ substrates.** **a**, A BF-TEM image of a Au heterodimer acquired at thermionic emission mode. **b**, UHS-CDF imaging of the nanoprism recorded at time zero. A model of the deformed nanoprism is shown in the inset. The green arch indicates the boundary formed due to bending deformation. **c**, Four individual frames (difference images) corresponding to P1-P4 marked in **d** (top panel) selected from a single oscillatory period. **d**, Temporal $I/I_0$ traces measured for the left ($S_L$) and right ($S_R$) halves (middle panel) of the nanoprism marked in **b** along polarization M1 indicated in **a**. Bottom panel: temporal $I/I_0$ trace for $S_R$ along polarization N1. The insets show the

power spectral density of the oscillatory section of the $I/I_0$ traces at $S_R$ after excitation by laser pulses with polarization M1 or N1.

## References


1. Zewail, A. H. Four-Dimensional Electron Microscopy. *Science* **328,** 187-193 (2010).
2. Arbouet, A., Caruso, G. M., & Houdellier, F. Ultrafast Transmission Electron Microscopy: Historical Development, Instrumentation, and Applications. In Advances in Imaging and Electron Physics **207**, 1–72 (2018).
3. Barwick, B., Park, H. S., Kwon, O.-H., Baskin, J. S. & Zewail, A. H. 4D Imaging of Transient Structures and Morphologies in Ultrafast Electron Microscopy. *Science* **322**, 1227-1231 (2008).
4. Park, H. S., Baskin, J. S., Barwick, B., Kwon, O.-H., & Zewail, A. H. 4D ultrafast electron microscopy: Imaging of atomic motions, acoustic resonances, and moiré fringe dynamics. *Ultramicroscopy* **110**, 7–19 (2009).
5. van der Veen, R. M., Kwon, O.-H., Tissot, A., Hauser, A. & Zewail, A. H. Single-nanoparticle phase transition visualized by four-dimensional electron microscopy. *Nat. Chem.* **5,** 395–402 (2013).
6. Cremons, D. R., Plemmons, D. A., Flannigan, D. J. Femtosecond electron imaging of defect-modulated phonon dynamics. *Nat. Commun.* **7**, 11230 (2016).
7. Cremons, D. R., Du, D. X., & Flannigan, D. J. Picosecond phase-velocity dispersion of hypersonic phonons imaged with ultrafast electron microscopy. *Phys. Rev. Mater.* **1**, 073801 (2017).
8. Kim, Y.-J., Lee, Y., Kim, K. & Kwon, O.-H. Light-induced anisotropic morphological dynamics of black phosphorus membranes visualized by dark-field ultrafast electron microscopy. *ACS Nano* **14**, 11383-11393 (2020).
9. Valley, D. T., Ferry, V. E. & Flannigan, D. J. Imaging Intra- and Interparticle Acousto-plasmonic Vibrational Dynamics with Ultrafast Electron Microscopy. *Nano Lett.* **16**, 7302-7308 (2016).
10. Kim, Y.-J., Jung, H., Han, S. W. & Kwon, O.-H. Ultrafast Electron Microscopy Visualizes Acoustic Vibrations of Plasmonic Nanorods at the Interfaces. *Matter* **1**, 1–15 (2019).
11. Danz, T., Domröse, T. & Ropers, C. Ultrafast nanoimaging of the order parameter in a structural phase transition. *Science* **371**, 371-374 (2021).
12. Reimer, L. & Kohl, H. Transmission electron microscopy physics of image formation. 5th ed. (Springer, Berlin, 2008).
13. Crut, A., Maioli, P., Del Fatti, N. & Vallée, F. Acoustic vibrations of metal nano-objects: time-

domain investigations. *Phys. Rep.* **549,** 1–43 (2015).

14. Ruan, C.-Y., Murooka, Y., Raman, R. K. & Murdick, R. A. Dynamics of size-selected gold nanoparticles studied by ultrafast electron nanocrystallography. *Nano Lett.* **7**, 1290-1296 (2007).
15. Liang, W., Schäfer, S. & Zewail, A. H. Ultrafast electron crystallography of heterogeneous structures: Gold-graphene bilayer and ligand-encapsulated nanogold on graphene. *Chem. Phys. Lett.* **542**, 8–12 (2012).
16. Hartland, G. V. Optical Studies of Dynamics in Noble Metal Nanostructures, *Chem. Rev.* **111,** 3858–3887 (2011).
17. Tchebotareva A. L. et al. Acoustic and optical modes of single dumbbells of gold nanoparticles. *ChemPhysChem* **10,** 111–114 ((2009)).
18. Miller, S. A., Womick, J. M., Parker, J. F., Murray, R. W. & Moran, A. M. Femtosecond relaxation dynamics of $Au_{25}L_{18}^-$ monolayer-protected clusters, *J. Phys. Chem. C* **113**, 9440–9444 (2009).
19. Calvo, F. Influence of size, composition, and chemical order on the vibrational properties of gold-silver nanoalloys. *J. Phys. Chem. C* **115**, 17730–17735 (2011).
20. Vasileiadis, T., Waldecker, L., Foster, D., Da Silva, A., Zahn, D., Bertoni, R., Palmer, R. E. & Ernstorfer, R. Ultrafast heat flow in heterostructures of au nanoclusters on thin films: atomic disorder induced by hot electrons. *ACS Nano* **12**, 7710−7720 (2018).
21. Li, D. S., Wang, Z. L. & Wang, Z. W. Revealing Electron-Phonon Interactions and Lattice Dynamics in Nanocrystal Films by Combining in Situ Thermal Heating and Femtosecond Laser Excitations in 4D Transmission Electron Microscopy. *J. Phys. Chem. Lett.* **9**, 6795-6800 (2018).
22. Burgin, J. *et al.* Time-resolved investigation of the acoustic vibration of a single gold nanoprism pair. *J. Phys. Chem. C* **112**, 11231-11235 (2008).
23. Ha, T. H., Koo, H.-J. & Chung, B. H. Shape-controlled synthesis of of gold nanoprisms and nanorods influenced by specific adsorption of halide ions. *J. Phys. Chem. C* **111,** 1123-1130 (2007).
24. Chen, L. et al. High-yield seedless synthesis of triangular gold nanoplates through oxidative etching. *Nano Lett.* **14,** 7201–7206 (2014).
25. Meena, S. K. et al. The role of halide ions in the anisotropic growth of gold nanoparticles: a microscopic, atomistic perspective. *Phys. Chem. Chem. Phys.* **18,** 13246–13254 (2016).
26. Anisimov, S. I., Kapeliovich, B. L. & Perelman, T. L. Electron Emission from Metal Surfaces Exposed to Ultrashort Laser Pulses. *J. Exp. Theor. Phys.* **66**, 375-377 (1974).
27. Nie, S., Wang, X., Park, H., Clinite, R. & Cao, J. Measurement of the electronic Gruneisen

constant using femtosecond electron diffraction. *Phys. Rev. Lett.* **96,** 025901 (2006).

28. Schäfer, S., Liang, W. X. & Zewail, A. H. Structural dynamics of nanoscale gold by ultrafast electron crystallography, *Chem. Phys. Lett.* **515,** 278–282 (2011).
29. dos Santos, W. N., de Sousa, J. A. & Gregorio, R. Thermal conductivity behaviour of polymers around glass transition and crystalline melting temperatures. *Polym. Test.* **32**, 987-994 (2013).
30. Lisiecki, I. et al. Coherent longitudinal acoustic phonons in three-dimensional supracrystals of cobalt nanocrystals. *Nano Lett.* **13,** 4914–4919 (2013).
31. Durvasula, L. N. & Gammon, R. W. Brillouin scattering from shear waves in amorphous polycarbonate. *J. Appl. Phys.* **50,** 4339−4344 (1979).
32. Luedtke, W. D. & Landman, U. Structure and Thermodynamics of Self-Assembled Monolayers on Gold Nanocrystallites. *J. Phys. Chem. B* **102,** 6566−6572 (1998).
33. Yi, C. et al. Vibrational coupling in plasmonic molecules. *Proc. Natl Acad. Sci. USA* **114,** 11621–11626 (2017).

## Methods

**Nanoparticle synthesis**. Au heterodimers were prepared based on a one-pot seedless approach originally designed for the synthesis of triangularly shaped Au nanoprisms[34]. In brief, 1.6 mL of 0.1 M cetyltrimethylammonium chloride (CTAC, 97%) was added to 8 mL of deionized water, followed by the addition of 75 μL of 0.01 M KI (99%), a mixture of 80 μL of 25.4 mM $HAuCl_4$ (99.995%) and 20.3 μL of 0.1 M NaOH, and 80 μL of 64 mM ascorbic acid (AA, 99.99%). The color of the reaction solution changed from pale yellow to colorless immediately after the introduction of AA. Finally, 10 μL of 0.1 M NaOH was added, followed by a quick shaking for several seconds. The solution color changed to purple, and finally blue within about 8 minutes, indicating the completion of the reaction. The synthesized solution was then diluted in deionized water, followed by centrifugation (~7100×g/10 mins) and sonication for 1-2 mins generally.

**UTEM experiments.** Our ultrafast TEM was built upon a 200 kV FEI Tecnai G20 UEM coupled with a Clark IMPULSE laser featuring a center wavelength of 1035 nm and pulse width 210 fs. UHS-CDF imaging was typically carried out with a convergence angle of ~2 mrad, an objective aperture of 4 mrad, and a pulse repetition rate of 200 kHz. All the $LaB_6$ filaments (150 μm with/without Guard rings) used in this study were purchased from APTech, Inc. The pulsed probe for UHS-CDF imaging was measured to contain about 55 electrons per timed packet - the level which can effectively prevent the Coulomb repulsion effect. Laser beams with the spot diameter

of ~67 μm and pump fluences of 1.4-2.8 mJ/cm$^2$ were employed for the excitation of structural dynamics within the samples. g(220) diffracting beams of Au nanoprisms were always selected for the dark field imaging because of their higher diffraction intensity and complete separation from substrate diffractions. For the vibrational interaction study, only the heterodimers with 1–2 nm internanoparticle gaps were investigated to minize the effect of weak intermolecular interactions in CTAC on energy transfer. Recording of time-lapse images were automated from a Digital Micrograph script that controls the delay stage movement through specially-compiled LabVIEW DLLs and the image acquisition based on parameters including time-delay range, time interval, exposure time, and accumulation times.

**Monochromatic EELS.** Localized surface plasmon resonance (LSPR) of Au nanoparticles shown in Supplementary Fig. 15 was measured through a Gatan dual EELS in an FEI double-aberration corrected Titan$^3$ G2 S/TEM incorporated with a monochromator. EELS spectrum images were acquired with an accelerated voltage of 60 kV, a convergence angle of 24 mrad, a collection angle of 18.9 mrad, and a dispersion of 0.01 eV per channel. A constant energy width of 0.1 eV (i.e., the instrument energy resolution) was adopted for extracting all the EELS maps corresponding to various LSPR modes.

**Optical cross-section calculations**. The calculation was carried out with COMSOL Multiphysics software (Wave Optics module). For modelling Au nanoprisms, a regular triangular prism with a side length of 68 nm (truncated with a fillet radius of 12 nm)

and a thickness of 15 nm was built by taking into account the actual geometry in Fig. 2a. As shown in Supplementary Fig. 19a, the incident plane wave travels along the nanoprism thickness (z-axis), linearly polarized along a bisector (y-axis). Wave equation (1) was adopted for the calculation of electric field distributions.

$$\nabla \times (\nabla \times E) - k_0^2 n^2 E = 0 \quad (1)$$

where $k_0$ denotes the wavenumber in vacuum, and $n$ the refractive index. A full field solution was first obtained by setting up two Port conditions, which function by either permitting specular reflection (Port 1) or absorbing transmitted plane waves (Port 2). Unphysical radiation reflection from external boundaries was absorbed by the addition of perfectly matched layer (PML) subdomains. With the calculated full field serving as the background field, the scattered field can be properly solved. This then enables the determination of optical cross sections for the nanoprisms and the nanospheres.

The optical constant of Au is taken from the data reported by Rakić, *et al*[35]. The properties of the surrounding medium of Au nanoparticles are, however, difficult to determine, including the thickness of CTAC, and optical constants of CTAC and nanoscale $Si_3N_4$ films. To quantitatively evaluate their effect on the photoabsorption, we assign the thickness of surfactant as 1 nm and its refractive index (n) as 1.41 (referring to the value of CTAB[36]), and then calculate the absorption cross sections of Au nanoprisms as a function of refractive indexes assigned to the substrates. By comparing them with the primary LSPR peak obtained in EELS experiments, we can determine the effective refractive index of $Si_3N_4$ substrates, 1.9, as demonstrated in

Supplementary Fig. 19b-c. The value is very close to the data reported by Luke, et al. (2.06-2.03 for the wavelength of 500-700 nm)[37]. Note that the calibrations can be made because the primary LSPR peak energy of Au nanoprisms is sensitive to the dielectric properties of surrounding medium.

**Two-temperature modelling.** Temperature evolution of metal nanoparticles induced by ultrashort laser excitation basically conforms to the two-temperature model approximation described by

$$C_e \frac{\partial T_e}{\partial t} = \nabla(k_e \nabla T_e) - \mathrm{G}(T_e - T_l) + \mathrm{S}(t) \quad (2)$$

$$C_l \frac{\partial T_l}{\partial t} = \mathrm{G}(T_e - T_l) \quad (3)$$

Here, the temperatures of electrons and lattices are represented by $T_e$ and $T_\mathrm{l}$, respectively. $C_e$, $k_e$, $C_l$, and $G$ denote the electron heat capacity ($71\times T_e$ $Jm^{-3}K^{-2}$), electron thermal conductivity ($318\times T_e/T_l$ $Wm^{-1}K^{-1}$), lattice heat capacity ($2.5\times10^6$ $Jm^{-3}K^{-1}$), and electron-phonon coupling constant ($2\times10^{16}$ $Wm^{-3}K^{-1}$), respectively[38-40]. *S(t)* is the laser source term, which is given by

$$S(t) = \frac{2\sqrt{ln2}C_{abs}E_p}{\sqrt{\pi}C_{phys}\delta\tau_p} \exp\left(-\frac{z}{\delta}\right) \cdot \exp\left(-\frac{4(ln2)\cdot(t-2\tau_p)^2}{{\tau_p}^2}\right) \quad (4)$$

where $C_{abs}$, $C_{phys}$, $E_p$, $\delta$, $\tau_p$ and z denote the absorption cross section, physical cross section of nanoparticles, incident laser fluence, penetration depth (20 nm), laser duration (210 fs) and the thickness of the sample (or the equivalent thickness, for a nanosphere, which is determined by dividing its volume by the area of a disk whose radius is equal to that of the nanosphere), respectively.

**Heat transfer simulations**. Using the heat transfer module in COMSOL, we simulate the temporal temperature evolution of Au heterodimers on $Si_3N_4$ substrates by setting

the initial temperature values of the nanospheres and nanoprisms to their respective lattice temperature maxima (i.e., 573 K and 496 K) and those of surfactants and substrates to room temperature (300 K). The Au nanoprisms and nanospheres are surrounded by 1 nm CTAC surfactants and supported on a $Si_3N_4$ block of 150×150×50 nm. Given that the areas of contact with the substrate could vary between different Au nanospheres, we evaluate this change based on a regular decahedron featuring a quasi-spherical shape. When the decahedron is orientated along its 5-fold axis, a nominally point contact with the substrate is formed (as is the case in Fig. 2). Two indentation depths of 0.1 and 0.2 nm (corresponding to the contact areas of 14 and 28 $nm^2$, respectively) are analyzed accordingly. In addition, a much larger contact status is also investigated for the case that one of the {111} facets of decahedron is located on the substrate. As illustrated in Supplementary Fig. 21b (inset), the area of contact (S1=210 $nm^2$) can be determined by assuming that the side length (OA) of the triangular facet is equal to the radius of nanosphere (22 nm). For the simulations, no phase change was considered and the thermal conductivity of bulk solid CTAC, 0.267 $Wm^{-1}K^{-1}$, was constantly used. The temporally varying temperatures are extracted from the centers of nanospheres and nanoprisms, and, for the surfactants at the nanosphere-nanoprism interface, from a 0.2 nm-wide region adjacent to the nanosphere (note that this side determines the time of full solidification due to its higher temperature).

**Data availability**

The data that support the findings of this study are available within the paper and the

Supplementary Information. Other relevant data are available from the corresponding author upon reasonable request. Source data are provided with this paper.

## Code availability

The codes that support the findings of this study are available from the corresponding author upon reasonable request.

## References


34. Chen, L. et al. High-yield seedless synthesis of triangular gold nanoplates through oxidative etching. *Nano Lett.* **14,** 7201–7206 (2014).
35. Rakic, A. D., Djurisic, A. B., Elazar, J. M. & Majewski, M. L. Optical properties of metallic films for vertical-cavity optoelectronic devices. *Appl. Opt.* **37**, 5271-5283 (1998).
36. Yu, C., Varghese, L. & Irudayaraj, J. Surface Modification of Cetyltrimethylammonium Bromide-Capped Gold Nanorods to Make Molecular Probes, *Langmuir* **23**, 9114-9119 (2007).
37. Luke, K., Okawachi, Y., Lamont, M. R. E., Gaeta, A. L. & Lipson, M. Broadband mid-infrared frequency comb generation in a $Si_3N_4$ microresonator, *Opt. Lett.* **40**, 4823-4826 (2015).
38. Hohlfeld, J. et al. Electron and lattice dynamics following optical excitation of metals. Chem. Phys. 251, 237–258 (2000).
39. Li, D. S., Wang, Z. L. & Wang, Z. W. Revealing Electron-Phonon Interactions and Lattice Dynamics in Nanocrystal Films by Combining in Situ Thermal Heating and Femtosecond Laser Excitations in 4D Transmission Electron Microscopy. *J. Phys. Chem. Lett.* **9**, 6795-6800 (2018).
40. Barwick, B., Park, H. S., Kwon, O.-H., Baskin, J. S. & Zewail, A. H. 4D Imaging of Transient Structures and Morphologies in Ultrafast Electron Microscopy. *Science* **322**, 1227-1231 (2008).

**Fig. 1**

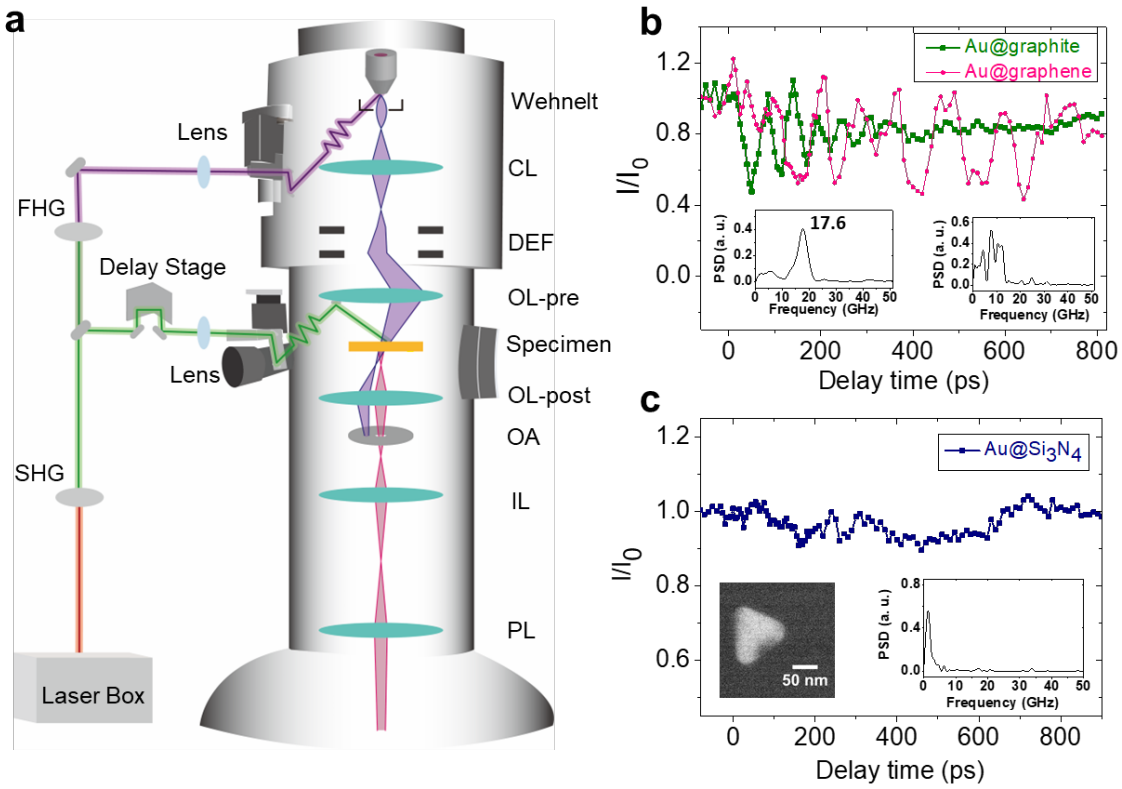
a
Wehnelt
CL
DEF
OL-pre
Specimen
OL-post
OA
IL
PL
Lens
FHG
Delay Stage
Lens
SHG
Laser Box
b
Au@graphite
Au@graphene
I/I0
17.6
PSD (a. u.)
Frequency (GHz)
Delay time (ps)
c
Au@Si3N4
50 nm
PSD (a. u.)
Frequency (GHz)
Delay time (ps)

**Fig. 2**

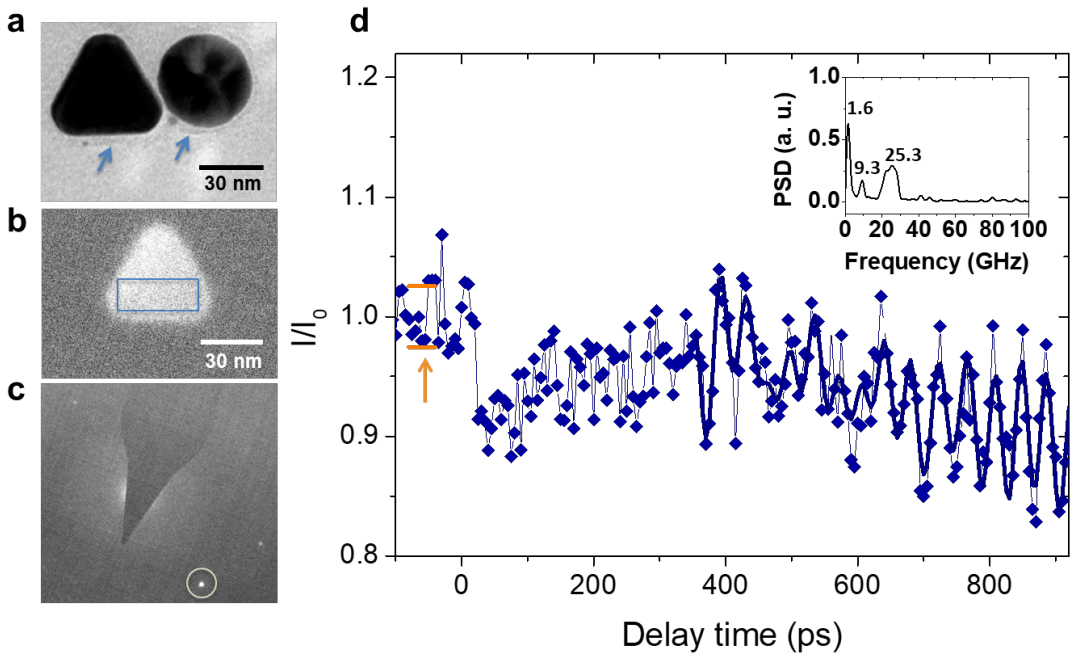
a
30 nm
b
30 nm
c
d
1.2
1.1
1.0
0.9
0.8
I/I0
0
200
400
600
800
Delay time (ps)
PSD (a. u.)
1.0
0.5
0.0
1.6
9.3
25.3
0 20 40 60 80 100
Frequency (GHz)

**Fig. 3**

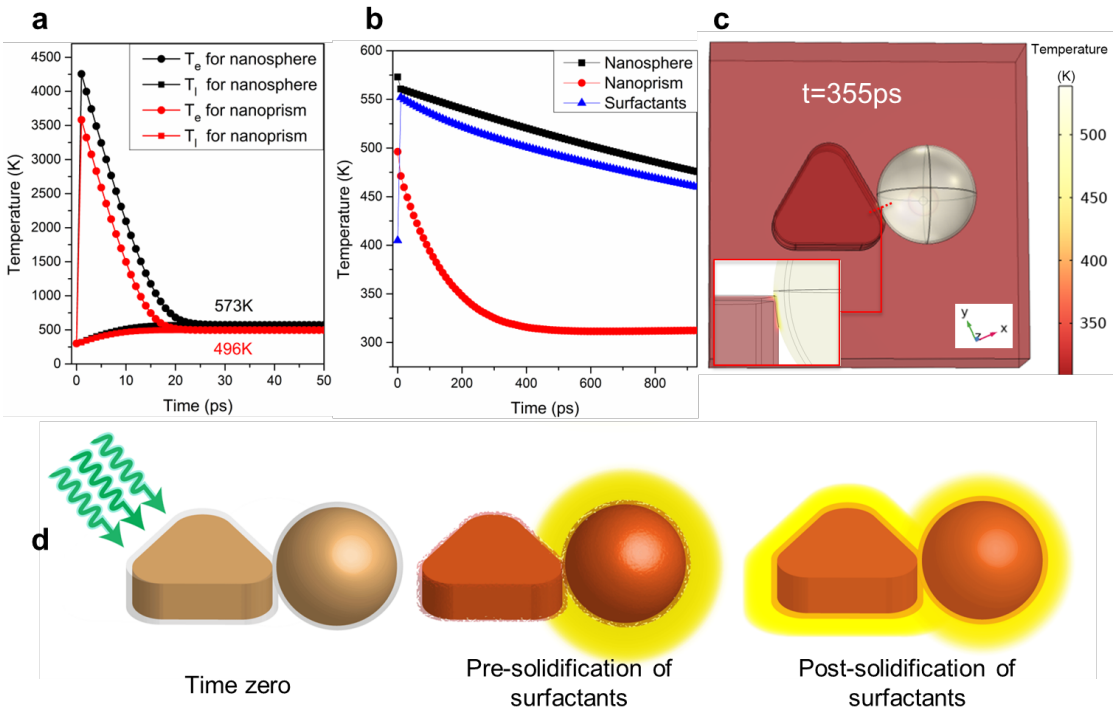
a
b
c
$T_e$ for nanosphere
$T_l$ for nanosphere
$T_e$ for nanoprism
$T_l$ for nanoprism
573K
496K
Temperature (K)
Time (ps)
Nanosphere
Nanoprism
Surfactants
t=355ps
Temperature
(K)
500
450
400
350
d
Time zero
Pre-solidification of surfactants
Post-solidification of surfactants

**Fig. 4**

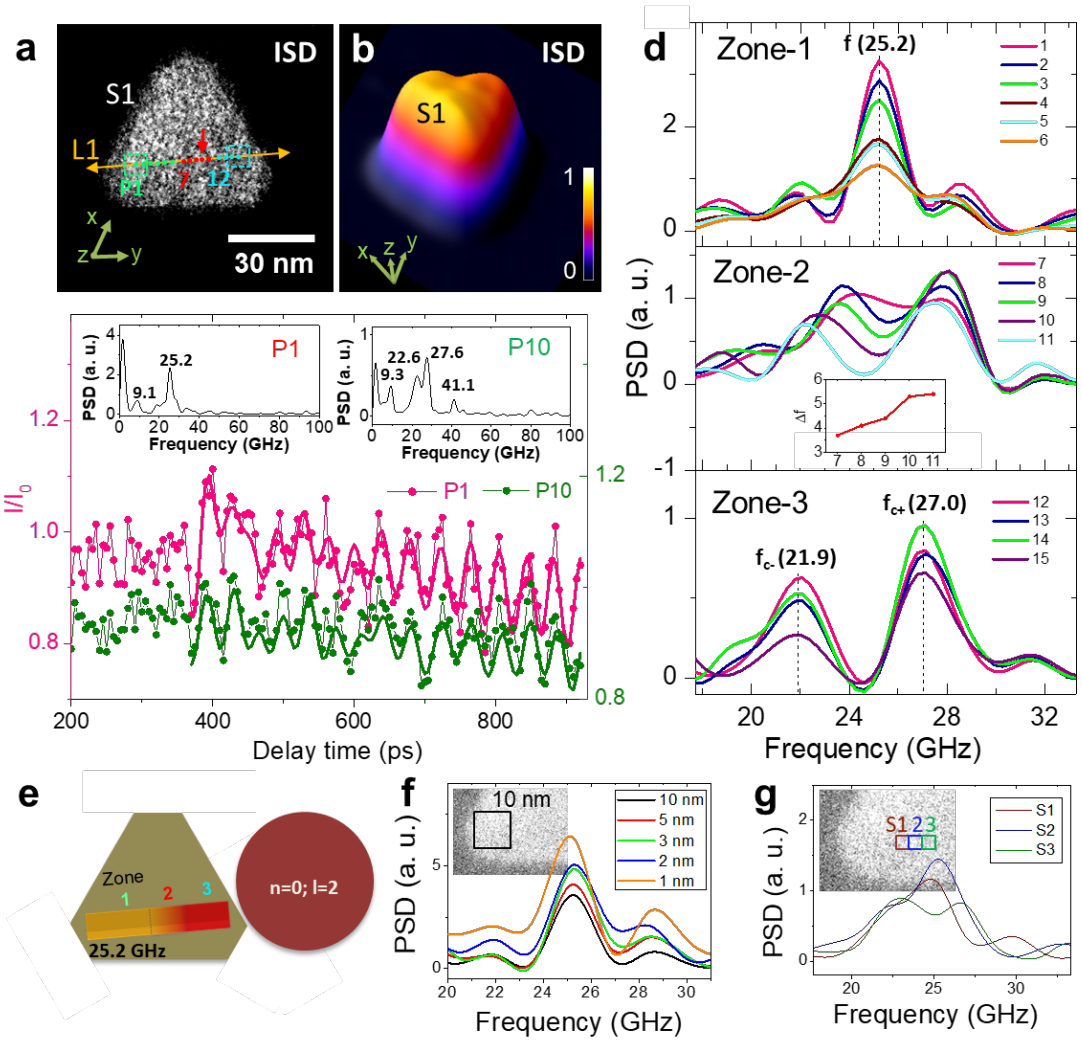
a
ISD
S1
L1
P1
L2
30 nm
b
ISD
S1
1
0
d
Zone-1
f (25.2)
Zone-2
Zone-3
$f_{c+}$ (27.0)
$f_{c-}$ (21.9)
PSD (a. u.)
Frequency (GHz)
P1
P10
25.2
9.1
22.6
27.6
9.3
41.1
I/I$_0$
Delay time (ps)
e
Zone
1
2
3
25.2 GHz
n=0; l=2
f
10 nm
5 nm
3 nm
2 nm
1 nm
PSD (a. u.)
Frequency (GHz)
g
S1 2 3
S1
S2
S3
PSD (a. u.)
Frequency (GHz)

**Fig. 5**

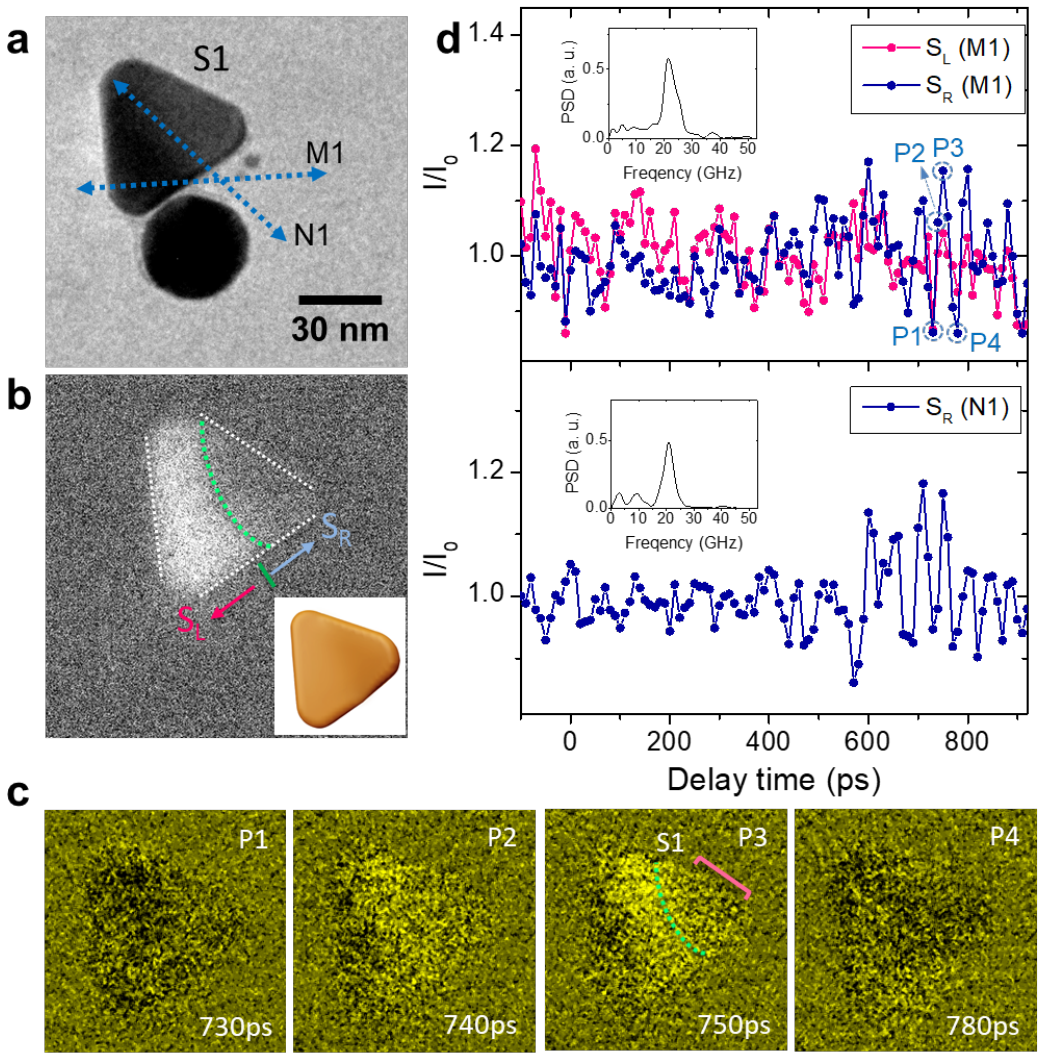
a
S1
M1
N1
30 nm
b
$S_R$
$S_L$
d
$S_L$ (M1)
$S_R$ (M1)
$S_R$ (N1)
PSD (a. u.)
Freqency (GHz)
P1
P2
P3
P4
I/I$_0$
Delay time (ps)
c
P1
730ps
P2
740ps
S1
P3
750ps
P4
780ps